JGR Space Physics

RESEARCH ARTICLE
10.1029/2023JA032157

Observations of Mesospheric Gravity Waves Generated by Geomagnetic Activity

V. L. Narayanan[1], C. Wright[1], M. Mlynczak[2], N. Hindley[1], A. Kavanagh[3], T. Moffat-Griffin[3], and P. Noble[1,3]

[1]Center for Climate Adaptation and Environment Research, University of Bath, Bath, UK, [2]NASA Langley Research Center, Hampton, SC, USA, [3]British Antarctic Survey, Cambridge, UK

Key Points:

- Geomagnetically forced gravity waves penetrate down to ~80 km only in the high latitude regions as revealed by Sounding of the Atmosphere using Broadband Emission Radiometry temperature data
- Summer high latitude mesosphere is less responsive for gravity wave generation due to geomagnetic activity
- Significant variability in the gravity wave response is noticed even between severe geomagnetic disturbances occurring in the same season

Correspondence to:
V. L. Narayanan,
narayananvlwins@gmail.com;
lnv23@bath.ac.uk

Citation:
Narayanan, V. L., Wright, C., Mlynczak, M., Hindley, N., Kavanagh, A., Moffat-Griffin, T., & Noble, P. (2024). Observations of mesospheric gravity waves generated by geomagnetic activity. *Journal of Geophysical Research: Space Physics*, *129*, e2023JA032157. https://doi.org/10.1029/2023JA032157

Received 10 OCT 2023
Accepted 26 MAR 2024

Author Contributions:
Conceptualization: V. L. Narayanan
Data curation: M. Mlynczak
Formal analysis: V. L. Narayanan
Funding acquisition: C. Wright, A. Kavanagh, T. Moffat-Griffin
Investigation: V. L. Narayanan, C. Wright
Methodology: V. L. Narayanan, P. Noble
Project administration: C. Wright, A. Kavanagh, T. Moffat-Griffin
Software: V. L. Narayanan, N. Hindley
Validation: M. Mlynczak, A. Kavanagh
Visualization: V. L. Narayanan, C. Wright
Writing – original draft: V. L. Narayanan
Writing – review & editing: V. L. Narayanan, C. Wright, M. Mlynczak, N. Hindley, A. Kavanagh, T. Moffat-Griffin, P. Noble

Abstract Gravity waves (GWs) play an important role in the dynamics and energetics of the mesosphere. Geomagnetic activity is a known source of GWs in the upper atmosphere. However, how deep the effects of geomagnetic activity induced GWs penetrate into the mesosphere remains an open question. We use temperature measurements from the SABER/TIMED instrument between 2002 and 2018 to study the variations of mesospheric GW activity following intense geomagnetic disturbances identified by AE and Dst indices. By considering several case studies, we show for the first time that the GWs forced by geomagnetic activity can propagate down to about 80 km in the high latitude mesosphere. Only regions above 55° latitudes show a clear response. The fraction of cases in which there is an unambiguous enhancement in GW activity following the onset of geomagnetic disturbance is smaller during summer than other seasons. Only about half of the events show an unambiguous increase in GW activity during non-summer periods and about one quarter of the events in summer show an enhancement in GWs. In addition, we also find that the high latitude mesopause is often seen to descend in altitude following onset of geomagnetic activity in the non-summer high latitude region.

Plain Language Summary Gravity waves (GWs) exist throughout the atmosphere and are crucial in the dynamics of the middle and upper atmosphere. A variety of processes are known to excite GWs at different altitudes. Above 100 km, space weather induced geomagnetic activity is an important source for the GWs. However, how deep such waves penetrate into the mesosphere, and in what latitude regions their effect is important remains unknown. In this work, we use SABER/TIMED satellite measurements of temperature between 2002 and 2018 to investigate this question. For the first time, we find that the geomagnetic activity forces mesospheric GWs only in the high latitude regions, where enhanced energy deposition occurs along magnetic field lines. Further, these GWs occur only above 80 km, and no unambiguous signature is seen at lower heights. Though damping is expected due to the increasing atmospheric density, this work identifies the altitude and latitude extent for such GWs forced by geomagnetic activity in the mesosphere. Further, there is a significant seasonality in the response such that summer hemisphere shows weakest GW generation due to geomagnetic activity. The mesopause height is also observed to descend sometimes during intense geomagnetic disturbances occurring in non-summer periods.

1. Introduction

Atmospheric gravity waves (GWs) are oscillations in the atmosphere spanning a wide range of spatio-temporal scales. Their horizontal sizes range from few 100 m to few 1,000 km, with vertical scales of few 100 m to few 10s of km, and time periods vary from about 5 min to several hours, upper limit determined depending on the latitude of observations (Fritts & Alexander, 2003). These waves are forced by different processes in different regions of the atmosphere and propagate away from the source region carrying energy and momentum. They play a crucial role in the vertical coupling of the atmosphere-ionosphere system. The importance of GWs in the upper mesosphere is now well recognized, and the counter-intuitive latitudinal temperature structure of the mesosphere is understood to result from GW driven circulation (Blanc et al., 2017; Smith, 2012). One of the earliest identified sources of upper atmospheric GWs was geomagnetic disturbances (Hunsucker, 1982; Oyama & Watkins, 2012) and it is well known that thermospheric GWs affect the ionosphere and manifest as traveling ionospheric disturbances, though the finer details of this plasma-neutral coupling process remains an active area of research (Zawdie et al., 2022). While the importance of geomagnetic activity as a GW source is well recognized for the thermosphere and E- and F-region ionosphere, the extent to which its dominance penetrates into the middle atmosphere is not properly investigated. It is expected that wave amplitudes will be damped when they propagate

downwards due to the exponentially increasing atmospheric density, but it remains unknown how deep geomagnetic activity induced GWs occur. Furthermore, prior to this study we do not know if this effect in the middle atmosphere is global or restricted only to the high latitudes. Neither we know about any seasonality in the mesospheric GW response to geomagnetic activity.

These aspects remain unknown due to the lack of sufficient data above 70 km at the required spatio-temporal scales. With increasing computational power, modeling of the atmosphere has improved significantly, but most such models focus on the troposphere and stratosphere. Several models are capable or providing physical parameters and chemical constituents of the mesosphere, yet GWs are not resolved and tend to be parameterized. For example, the Whole Atmosphere Community Climate Model (WACCM) (Gettelman et al., 2019; Smith et al., 2017), and the Ground-to-topside Atmosphere Ionosphere model for Aeronomy (GAIA) (Jin et al., 2011). Both can include aspects of ionospheric electrodynamics to varying degrees. The Thermosphere–Ionosphere–Mesosphere Electrodynamics–Global Circulation Model (TIME-GCM) is a widely used model in upper atmosphere - ionosphere studies. It differs from the above mentioned models in that the lower boundary of the model is at stratospheric heights (Roble & Ridley, 1994). Yet, TIME-GCM also uses GW parameterization and suffers from the lack of required spatio-temporal resolutions to study GW generation from geomagnetic activity. Further, none of these models capture finer variations in the temperature and wind in the mesosphere at the required resolution (Harvey et al., 2022; Hindley et al., 2022; Noble et al., 2022; Siskind et al., 2019; Stober et al., 2021).

Ground based measurements are available up to about 100 km but they are typically restricted by geographical location which make it impossible to understand the effects in the global context. An important drawback for ground based radio remote sensing of mesospheric neutral wind measurements is that the measured winds are significantly affected by the ionospheric variability occurring above 90 km (Ramkumar et al., 2002; Reid, 2015). Geomagnetic activity often results in increased contamination from the ionospheric processes at heights above 90 km. Airglow measurements can also provide information about the upper mesosphere, specifically imaging technique is capable of observing different types of waves and instability structures (e.g., Narayanan et al., 2012). However, in the high latitudes, auroral contamination makes imaging of GWs nearly impossible during geomagnetically active times hindering a study of mesospheric GW response using airglow imagers. Therefore, it is important to combine different type of ground based measurements to properly address this problem, for example, combining radar, airglow and lidar measurements. Co-existence of such diverse measurements from single location is extremely rare. Gathering different types of ground based mesospheric measurements from multiple sites to study the mesospheric GW variability corresponding to geomagnetic activity has not been accomplished yet.

Space based remote sensing from artificial satellites provide an opportunity to measure the atmosphere globally. Many limb sounding and nadir viewing swath measurements of atmospheric parameters like temperature and radiance have been used in the past to study GWs (Alexander et al., 2008; Ern et al., 2004; John & Kumar, 2012; Wright et al., 2011, 2016). However, most satellite measurements provide information on neutral atmosphere only to ∼70 km altitude from the surface. Space based ionospheric measurements are often made in the F-region heights. As a result, the region from 70 to 120 km is unfortunately not well measured with satellite remote sensing.

There are some noticeable exceptions to this limited coverage of the 70–120 km range like the Wind Imaging Interferometer (WINDII) (Shepherd et al., 2012) and the High Resolution Doppler Imager (HRDI) payloads (Fleming et al., 1996; McLandress et al., 1996) onboard the Upper Atmosphere Research Satellite (UARS) satellite. UARS flew in the early 1990s, but the satellite inclination was low enough that high latitude wind measurements were not available. Further, the measurements had a day-night difference in the altitude coverage as well. Sounding of the Atmosphere using Broadband Emission Radiometry (SABER) and TIMED Doppler Interferometer (TIDI) are the payloads designed to measure temperature and winds, respectively, and flown onboard Thermosphere - Ionosphere - Mesosphere Energetics and Dynamics (TIMED) satellite (Mertens et al., 2009; Remsberg et al., 2008; Wu & Ridley, 2023). SABER measures temperature and some minor constituents. TIDI measures four separate line of sight winds and it appears to have problems in getting proper vector wind estimates continuously (Wu & Ridley, 2023). The Solar Occultation For Ice Experiment (SOFIE) onboard Aeronomy of Ice in the Mesosphere (AIM) satellite measures temperatures but only during sunrise and sunset hours of each orbit leaving only ∼30 profiles at different locations in a day (Gordley et al., 2009). Recently, the Ionospheric CONnection explorer (ICON) mission had the Michelson Interferometer for Global High-resolution Thermospheric Imaging (MIGHTI) payload capable of measuring neutral winds but the satellite is of a low

inclination orbit not covering middle and higher latitude regions (Harding et al., 2017). Among these, SABER temperatures have been measured continuously from January 2002 with an altitude coverage from upper troposphere to 110 km and near-global spatial coverage. Therefore, SABER is suitable for studying the importance of space weather sources in generating GWs into the middle atmosphere. The temperatures are retrieved both during day and night with reliable error estimates upto about 110 km (García-Comas et al., 2008; Remsberg et al., 2008). Hence we use SABER data for this study and the analysis method is explained in the next section.

This is the first study to investigate mesospheric GWs forced by geomagnetic activity in a global context. This is an important component of space weather impacts on the middle atmosphere. Further, the observational results provided here are expected to help formulate model improvements for the upper mesospheric region.

2. Data Analysis

2.1. Event Identification

Since our aim is to understand the role of geomagnetic activity in the forcing of mesospheric GWs, we ensure only the strongest events are selected in order to study the effects unambiguously. We use the Auroral Electrojet (AE) index and Disturbance storm-time (Dst) index to identify the events. AE index is widely used to study the auroral activity and substorm occurrences. AE index is derived from a set of magnetometers in the northern hemispheric auroral region. The Dst index is derived from a set of low-mid latitude magnetometer stations and mainly indicates the intensification of the ring current. Dst index is used to identify the geomagnetic storms. First, we focused on major geomagnetic storms having minimum Dst ≤ -200 nT and those extreme events with a high threshold of AE $\geq$ 1500 nT. This identified 24 events between 2002 and 2018. Once the AE index reaches a maximum beyond 1500 nT, we find the time when the AE index start to rise above 300 nT. We define this time as start of the event. Short period fluctuations of AE < 300 nT are allowed if occurring for less than 8 continuous hours, so that rapid fluctuations before a major event are accounted for.

To improve statistics and check that the results from detailed event-based analysis hold for relatively weaker geomagnetic disturbances, we also identified all events with maximum AE $\geq$ 1000 nT. The start for such events is taken as the AE index reaching 300 nT and remaining quasi-continuously high. By quasi-continuous, we allow fluctuations below 300 nT but not for $\geq$8 hr. Often the AE indices will fluctuate above 1000 nT a few times during such intense geomagnetic activity periods. We merge such fluctuations into a single event. In this way, 248 events were identified to perform a seasonal and hemispherical statistics between 2002 and 2018.

2.2. SABER/TIMED Data Analysis

We use temperature measurements from the SABER instrument onboard the TIMED satellite obtained between 2002 and 2018. The instrument measures limb radiances between 1.27 and 16.9 μm in 10 channels from which temperature and other minor species concentrations are retrieved. Detailed description of the instrument and retrievals can be found elsewhere (Esplin et al., 2023). The latitudinal coverage alternates between 83°N–52°S and 52°N–83°S every 60–63 days, resulting in coverage of high latitudes only in one of the hemispheres at any given time. The SABER scan is designed such that adjacent profiles are separated alternatively by ∼250 km and ∼450 km distances along the track at the upper mesospheric tangent heights. The instantaneous field of view of the instrument is ∼2 km but the retrievals are made at a finer spacing of about 0.4–0.5 km altitude steps. We apply a 2 km smoothing and resample the data at 1 km vertical intervals. Three such successive profiles are shown in Figures 1a–1c.

In SABER data, each data point in a profile is associated with a latitude, longitude, solar local time (SLT) and universal time (UT). We average these values for each profile between 15 and 110 km heights to represent a mean location and time for the profile. To obtain a background for a particular temperature profile, the adjacent profiles along the satellite track are taken together and a 7 km vertical running average is made on the three profile combination. This background profile is shown in Figure 1d. The thin dotted line shows the original profile. By subtracting the estimated background profile from each profile, we obtain temperature perturbations that are predominantly contributed by GWs (Figure 1e). For background estimation, 7 km was selected for the running average in the vertical after considering a range of step sizes. For smaller step sizes, many GWs will be included in the background and when it is larger, the mesopause and any sharp inversion layers will be smoothed out in the background temperature unrealistically. The latter will generate large perturbation temperatures that are not real

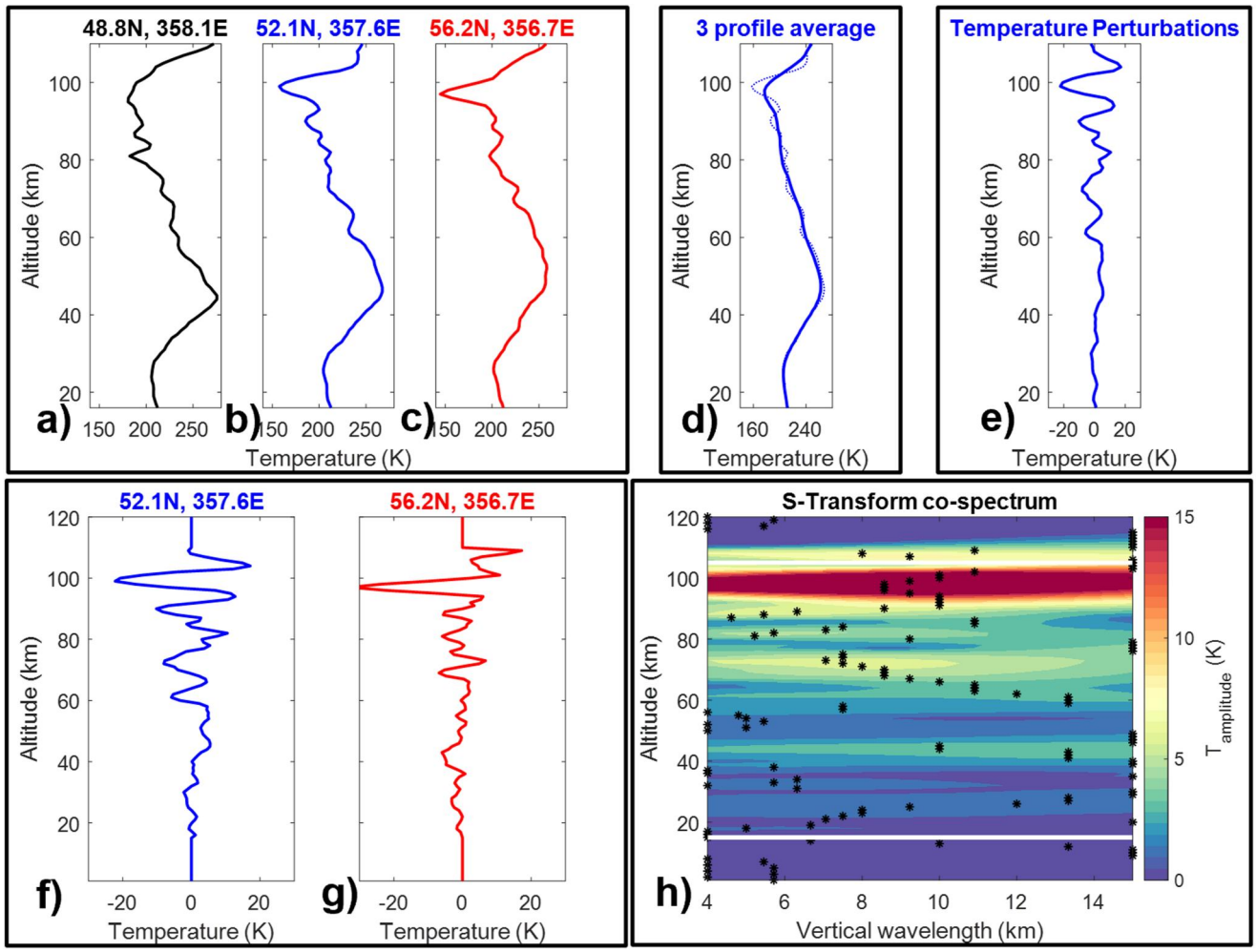

Figure 1. (a)–(c) Three adjacent temperature profiles at 1 km vertical spacing after applying 2 km smoothing (see text for details), (d) Thick line shows the 7 km Average of the three profiles shown in panels "a–c" which is taken as the background for the center profile given in panel "b" (also shown with dotted lines), (e) Temperature perturbations obtained after subtracting the background, (f)–(g) Zero padded adjacent temperature perturbation profiles, (h) Amplitude co-spectra of S-Transform of the profiles shown in panels "f–g". The stars shows the maximum amplitude wave at each altitude which is considered for further calculations of GWPE and MF.

when subtracting the estimated background temperature profile. At the same time, we note that 7 km coincides with mean scale height. When making background temperature estimations in this way, the intrinsic assumption is that the background is smooth over about 700 km in the horizontal, that is, the average distance covered between 3 profiles in the along-track direction.

An S-transform analysis is applied to temperature perturbation profiles (Figure 1e) following past works (e.g., Alexander et al., 2008; Hindley et al., 2019; Stockwell et al., 1996; Wright et al., 2016). Hindley et al. (2019) discusses in detail the S-transform calculation that has been adopted herein. The complex output of S-transform of each profile is multiplied by the complex conjugate of the adjacent profile's S-transform to obtain a complex co-spectrum. Figures 1f and 1g shows the adjacent temperature perturbation profiles zero padded to reduce edge effects resulting in the amplitude co-spectrum shown in Figure 1h. The maximum values of the co-spectrum at each altitude is assumed to represent the dominant wave at that particular altitude. From the magnitude of the complex co-spectrum peak, we obtain the square of the wave amplitude in temperature. By dividing the phase with the distance between adjacent profiles, we obtain the horizontal wavenumber of the dominant wave (see Alexander et al. (2008); Wright and Gille (2013) for more details). The corresponding frequency of the co-spectral peak gives the vertical wavenumber. In this way, we obtain an estimate of the amplitude of the dominant wave perturbation, its vertical and horizontal wavenumbers. Note that we restrict the vertical scales of the

S-transform to 4–15 km. Because we study geomagnetic disturbances spanning a few days, the longitudinal coverage is sparse and hence we use zonal average of the GW parameters in our study.

2.3. Gravity Wave Potential Energy and Momentum Flux Calculations

From the estimated wave parameters, gravity wave potential energy (GWPE) and momentum fluxes are obtained from the following relations.

$$E_P = \frac{1}{2}\frac{g^2}{N^2}\left(\frac{T'}{\overline{T}}\right)^2 \tag{1}$$

$$M_f = \frac{\rho}{2}\frac{\lambda_v}{\lambda_h}\frac{g^2}{N^2}\left(\frac{T'}{\overline{T}}\right)^2 = E_p\rho\frac{\lambda_z}{\lambda_h} \tag{2}$$

where, E_P and M_f represents GWPE per unit mass and the momentum flux per unit volume (vertical flux of horizontal momentum) respectively (Ern et al., 2004). g and ρ stand for acceleration due to gravity and density respectively. We used the densities provided by SABER data and account for the variation of g with height. λ_h and λ_v represent the horizontal and vertical wavelengths obtained from cospectral analysis. T' is the perturbation temperature and $\overline{T}$ is the background temperature. We can calculate GWPE using (a) the temperature perturbations obtained as the amplitude of spectral analysis which correspond to the dominant wave mode at a height and pair of profiles (the temperature value indicated by the stars in Figure 1e as done in Alexander et al. (2008), for example), and (b) also using the raw temperature perturbations obtained after subtracting the background temperature estimates assuming the contributions from turbulence and tides are negligible compared to GWs. While the latter assumption is a rudimentary one, the variabilities appear to be similar in both the potential energy estimates and we prefer to use the ones calculated from the spectral analysis. The term N in the equation is the buoyancy frequency calculated from the measured temperature and its gradient as below,

$$N^2 = \frac{g}{\overline{T}}\left(\frac{d\overline{T}}{dz} + \frac{g}{C_P}\right) \tag{3}$$

where g/C_P is the dry adiabatic lapse rate with C_P, the specific heat at constant pressure taken as 1,005 $\mathrm{Jkg^{-1}K^{-1}}$. This is justified because the topmost region considered in our study is still around the turbopause and the atmosphere remains well mixed. We divide the momentum flux by atmospheric density to result in units of $\mathrm{m^2/s^2}$, which is momentum flux per unit mass. In this work we will refer to momentum flux per unit mass as momentum flux (MF) for brevity. Note that this parameter is dimensionally similar to the wind variances due to GWs. This aids in better visualization of variation with altitude because momentum flux per unit volume usually given in units of Pa decrease exponentially with height.

In the above discussion, the GWs identified are affected by the instrument observational filter effect, that is, the sensitivity of a measurement technique to a range of GW frequencies and wavelengths. No instrument is capable of measuring the whole spectrum of GWs. The observational filter of SABER is estimated in Figure 9 of Wright et al. (2016). Because the cospectrum is computed in the satellite's along-track direction, any wavevector oriented orthogonal to the track will not be observed. For a wave propagating in an arbitrary direction, the wave vector's projection along the satellite track is identified and hence the measured horizontal wavenumber is less than the real wavenumber in the horizontal indicating that the measured momentum flux will be less as well. Hence, we are measuring only a part of the momentum flux from a portion of the GW spectrum that is restricted by observational filter effect of the instrument. Therefore, we will not focus on the absolute quantification and the magnitude of the GW momentum fluxes. Rather we will focus on the relative changes and variations before, during and after the geomagnetic activity in this work. This realization also enables us to adopt a computationally efficient way to study the wave variabilities by selecting the dominant wave signature from the S-Transform instead of selecting waves above a particular threshold or significance level. This approach is widely used (Alexander et al., 2008; Hertzog et al., 2012; McDonald, 2012; Wright & Gille, 2013; Wright et al., 2016).

To check if there is an unambiguous enhancement following geomagnetic activity, we calculate GWPE and MF for 48 hr before and after the start of the event. This is not based on UT days but is a zonal average of the data for

Table 1
Seasons and Number of Events Identified

	Northern hemisphere			Southern hemisphere		
		No. of. events			No. of. events	
Seasons	Duration	AE ≥ 1500 nT	AE ≥ 1000 nT	Duration	AE ≥ 1500 nT	AE ≥ 1000 nT
Winter	22 Oct–21 Feb	4	34	22 Apr–21 Aug	7	57
Vernal	22 Feb–21 Apr	1	14	22 Aug–21 Oct	2	19
Summer	22 Apr–21 Aug	4	43	22 Oct–21 Feb	3	19
Autumn	22 Aug–21 Oct	1	28	22 Feb–21 Apr	2	34

48 hr before and after the hour of onset. Note that as described in Section 2.1, the start is when the AE reaches and quasi-continuously stays above 300 nT. The percentage change (C) is evaluated as,

$$C = \frac{(P_{aft} - P_{bef})}{P_{bef}}.100 \quad (4)$$

where, P_{bef} and P_{aft} are the 48 hr averages of GWPE or MF before and after the onset, respectively.

In order to obtain a statistically valid threshold to decide if there is an unambiguous enhancement in GW activity, we created a database of background variability from 7,000 randomly selected points. The year, month, date and hour are selected randomly. The percentage change of GWPE and MF are calculated for these 7,000 points. Note that we analyze SABER measurements for 17 years from 2002 to 2018 having a total of only about 6,200 days. Because we also randomly select the time, calculating for 7,000 points is possible and it ensures removal of any biases that would arise from UT dependence in the background variations if we did a simple day-to-day variability calculation centered at a particular UT hour. No geomagnetic indices are considered when randomly sampling the start times and hence a small portion of these random variations may have also occurred around geomagnetically active periods. The 85th percentile of this data set is taken as a threshold for identifying if there is an unambiguous increase in GW acuity. The 85th percentile falls near 10%. So, when the mean C between 85 and 100 km altitudes is above +10% for either GWPE or MF, it is considered to indicate an unambiguous generation of GW due to the geomagnetic activity.

2.4. Seasonal Separation

We consider a month on either side of the equinox days as equinoctial periods: February 22–April 21 and August 22–October 21. Periods outside these ranges are considered to represent either summer or winter solstice based on the high latitude hemisphere covered by the satellite. Table 1 shows the periods considered as summer, winter and equinoxes in this study along with the number of events identified for different AE thresholds.

3. Results

3.1. Case Studies

3.1.1. Winter Observations

Figures 2a and 2b shows the Dst and AE indices around one of the strongest geomagnetic event of this century, which started on 29 October 2003, sometimes referred to as Halloween storm of 2003. The event was a geomagnetic superstorm with a double dip in the Dst index plummeting below −350 nT and with an AE index crossing 2000 nT. Figures 2c–2f shows the daily zonal mean of GW parameters from 90 to 100 km altitude separated into 5° latitude bins. GWPE, Temperature perturbations and MF (panels (c–e)) show a clear enhancement in wave activity poleward of 55°N during geomagnetic disturbance (see Doy 302–306). Vertical wavelengths (Figure 2f) show an enhancement during the geomagnetic event around the same latitude regions where an enhanced wave activity is noticed. Note that these vertical wavelengths are also zonal averages in 5° latitudinal bins. This indicates that relatively longer vertical wavelength GWs are observed following the storm.

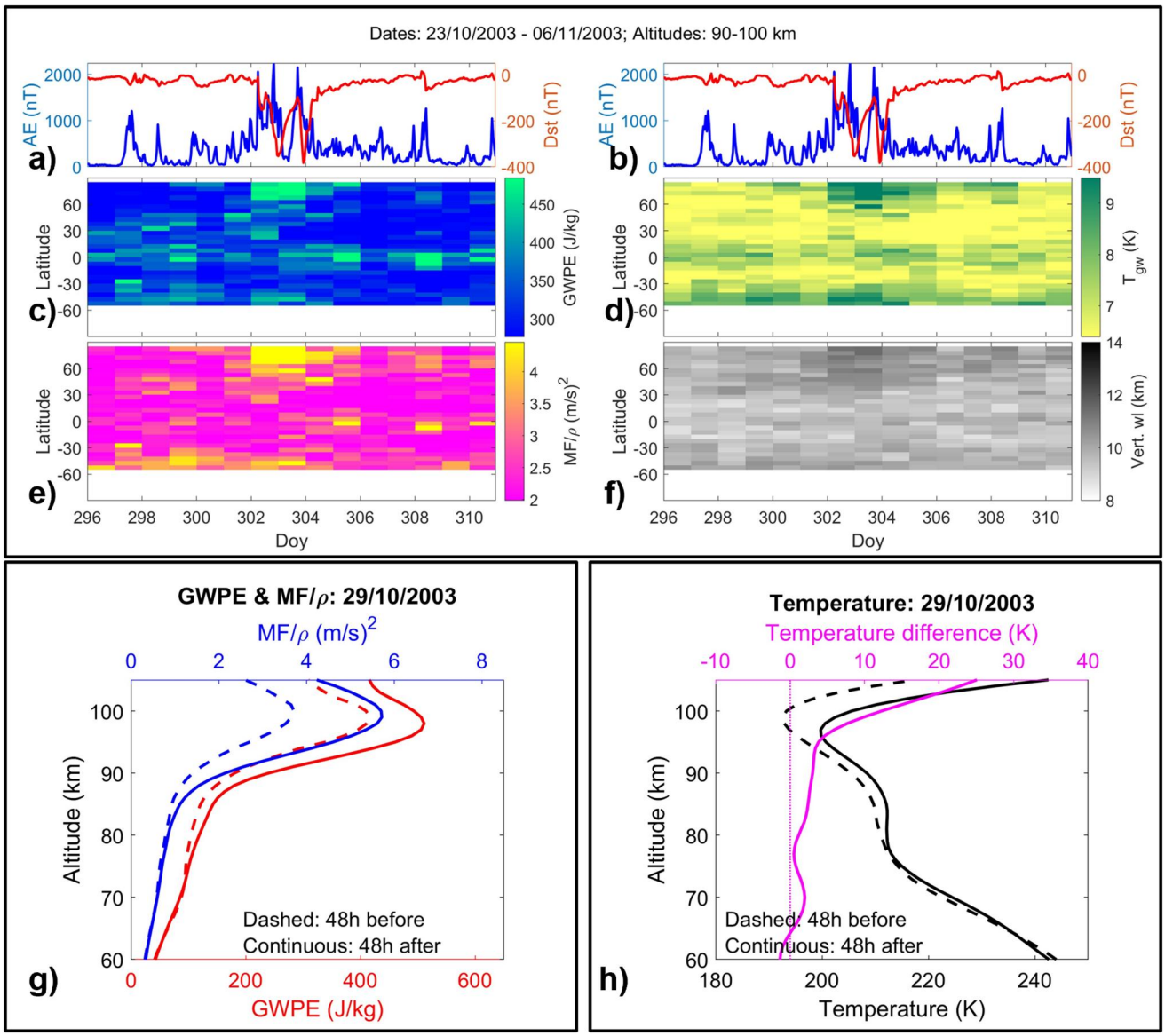

Figure 2. Geomagnetic superstorm of 29 October 2003. (a) and (b) AE and Dst indices, (c) GWPE per unit mass, (d) Temperature perturbations before subjecting to spectral analysis, (e) MF per unit mass, (f) Vertical wavelengths. All the parameters in panels (c)–(f) are daily longitudinal averages at 5° latitude bins. (g) Altitude profiles of average GWPE and MF from 60 to 90° magnetic inclinations in the Northern hemisphere for 48 hr before and after onset of geomagnetic event, and (h) Zonal average temperature profiles from 60 to 90° magnetic inclinations for 48 hr before and after the onset of geomagnetic event in black, and the temperature difference in magenta (after–before).

Figure 2g shows the altitude profiles of GWPE and MF obtained 48 hr before (dashed lines) and 48 hr following the storm onset (continuous lines). The region spanning magnetic inclination of 60°–90° in the Northern hemisphere are averaged herein to obtain the figure since the satellite coverage is in that hemisphere. Averaging with respect to the magnetic inclination values instead of geographic latitude band is necessary since energy deposition during geomagnetic disturbances directly occur in the regions with higher magnetic inclinations (and therefore higher magnetic latitudes). The magnetic inclination values at 100 km altitude are obtained from IGRF 13 model (Alken et al., 2021). Figure 2g shows an unambiguous enhancement of the wave activity from about 80 km following the geomagnetic storm. For the first time, this clearly shows the depth to which dynamic effects of geomagnetic activity penetrates directly.

Figure 2h shows the 48 hr average of temperature profiles before and after the storm onset plotted in black, calculated for the same geographic region as in Figure 2g. This shows the effect of intense geomagnetic activity

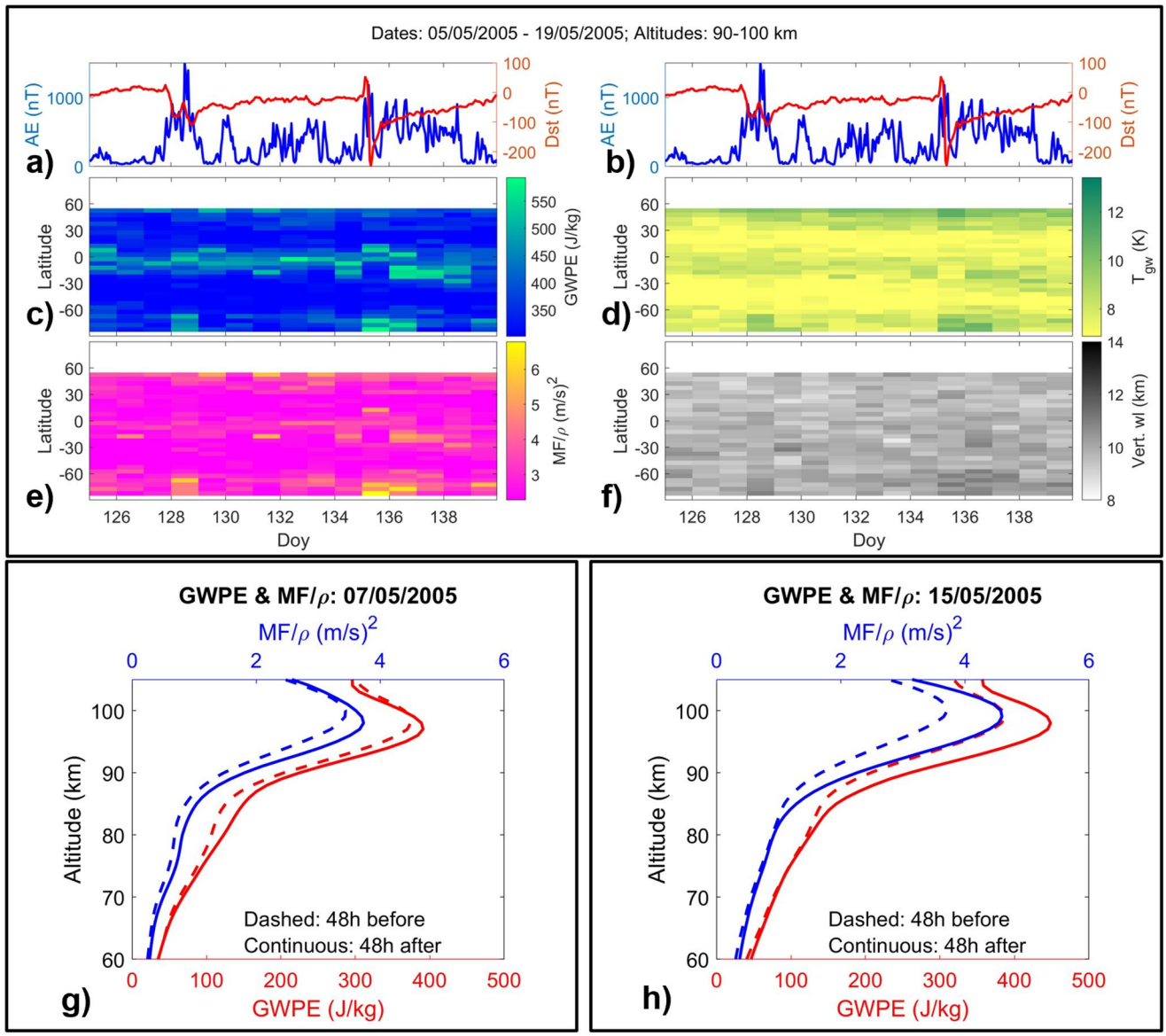

Figure 3. Events of 7 and 15 May 2005. (a) and (b) AE and Dst indices, (c) GWPE, (d) Temperature perturbations without subjecting to spectral analysis, (e) MF, (f) Vertical wavelengths. (g) and (h) Altitude profiles of average GWPE and MF from 60 to 90° magnetic inclinations in the Southern hemisphere for 48 hr before and after the onset respectively for 7 and 15 May 2005.

on the upper mesospheric temperature. There is a heating due to the enhanced geomagnetic activity as can be seen from the higher temperature values post storm onset. This is better visualized with the magenta curve showing the difference between temperatures after and before the storm onset, that is, difference between the continuous and dashed black curves. In addition, the altitude of the mesopause descends as a result of the heating as revealed by the black lines in Figure 2h.

Figure 3 show the results for two events during May 2005. During this period SABER was covering Southern high latitudes and hence these were observed in winter. The first event is a compound substorm which started on 7 May and continued until 8 May 2005. There was only a moderate geomagnetic storm during this period as can be inferred from the Dst index reaching a minimum close to −100 nT. The second event is that of the major geomagnetic storm of 15 May 2005 (day of the year (Doy) 135) when the Dst indices reached below −200 nT (Figures 3a and 3b). Though the peak value of AE is higher during 7–8 May 2005, the event of 15 May 2005 continued for about 3 days and resulted in one of the severe geomagnetic storms and hence is the

stronger prolonged event amongst the two. From the GWPE, MF and temperature perturbations (Figures 3c, 3e, and 3d), it is clear that there is an enhanced wave activity on 8 May 2005 (Doy 128) and 15 and 16 May 2005 (Doy 135 and 136). Similar to the case of 29 October 2003, the vertical wavelengths show a coincident enhancement (Figure 3f) during both the events in the high latitudes. Another noticeable feature in Figures 3c–3f is that the period of 9–14 May 2005 is not quiet. Though the AE index has not reached extremely high values of 1000 nT, the period has had significant geomagnetic substorm events and auroral activity. There are intermittent weaker enhancements in GW activity as well, for example, on days 132 and 133. These observations confirm that intense substorms like that of 7–8 May 2005 also generate GWs into the mesosphere. This implies that the physical processes behind the GW generation are similar for major geomagnetic storms and strong substorms.

Figures 3g and 3h respectively show the altitude profiles of average GWPE and MF for the compound substorm of 7 May 2005 and major geomagnetic storm of 15 May 2005. These profiles are averages between magnetic inclination of −60°–90° in the Southern Hemisphere. The enhancement in GW activity is larger for the stronger event of 15 May 2005. Similar to the event of 29 October 2003 (Figure 2) and that of 7 November 2004 (not shown), a clear increase in GW activity is seen above 80 km for both these events observed during winter. It appears that the direct penetration of GWs ceases around 80 km and hence geomagnetic activity is an important source only in the upper mesosphere. In addition, the neutral temperature behavior for these two events (not shown) is similar to that of the 29 October 2003 case (Figure 2h) in that the mesopause descended along with higher temperature values post storm onset. Similar descent of mesopause was also noticed during severe storm of 7 November 2004 observed by SABER above the northern high latitudes (not shown).

3.1.2. Summer Observations

Figure 4 shows three events in June - July 2005 with onset dates of 12 June (Doy 163), 22 June (Doy 173) and 09 July (Doy 190), respectively. All three events had large AE indices indicating very strong substorm activity, but were only moderate geomagnetic storms with Dst around −100 nT (Figures 4a and 4b). Note that generally there is enhanced GW activity at high latitudes during summer irrespective of geomagnetic activity associated enhancements (Figures 4c–4f, above 60°N, later it will be shown with GW climatology in Figure 9 as well). Figures 4g–4i shows the altitude profiles of the average GWPE and MF between 60°–90° inclination angles for the three events. For the first event of 12 June 2005, there is a clear enhancement in the wave activity above ∼88 km (Figure 4g). For the second event beginning on 22 June 2005, there is an enhancement in wave activity only above 94 km (Figure 4h). This event does not show a +10% change between 85 and 100 km according to our threshold. Evidently, the magnetic activity levels for 22 June event was weaker compared to that of 12 June 2005 (Figures 4a and 4b).

The third case of 9 July 2005 does not show any enhancement in GW activity (Figures 4i and 4c–4e). However, there is a weak enhancement in average vertical wavelengths for the 9 July 2005 case (Figure 4f). It appears as if the geomagnetic activity contributed to some wave generation indicated by vertical wavelength enhancement similar to other cases. Nevertheless, the pre-existing wave activity and its variability during summer masks the contribution from geomagnetic activity. Such a scenario could explain the lack of enhanced wave activity in the averaged wave properties like GWPE and MF while there is an enhancement in the averaged vertical wavelength. Alternatively, it is likely that the power of pre-existing GW variation was already large during this summer event so that the contribution from geomagnetic activity falls below background levels except in the vertical wavenumber. Figures 4a–4f has been terminated on 14 July 2005 (Doy 195) right at the end of the multi-night compound substorm event of 9 July 2005 due to a change in SABER latitude coverage.

These events are observed in summer high latitudes where the mesopause occurs below 90 km (Figures 4j–4l). Note that the mesopause height during summer is not affected following onset of geomagnetic activity contrary to other events reported earlier. Nevertheless, the extent of heating during summer is comparable to other seasons as seen from the temperature difference profiles after and before the geomagnetic disturbances (magenta curves). Interestingly, the heating during 12 June and 9 July 2005 is comparable in strength but the former shows an enhanced GW forcing below 100 km while the latter does not. Thus, the summer high latitudes appear to respond in a different manner to the geomagnetic activity as seen above within a span of 30 days.

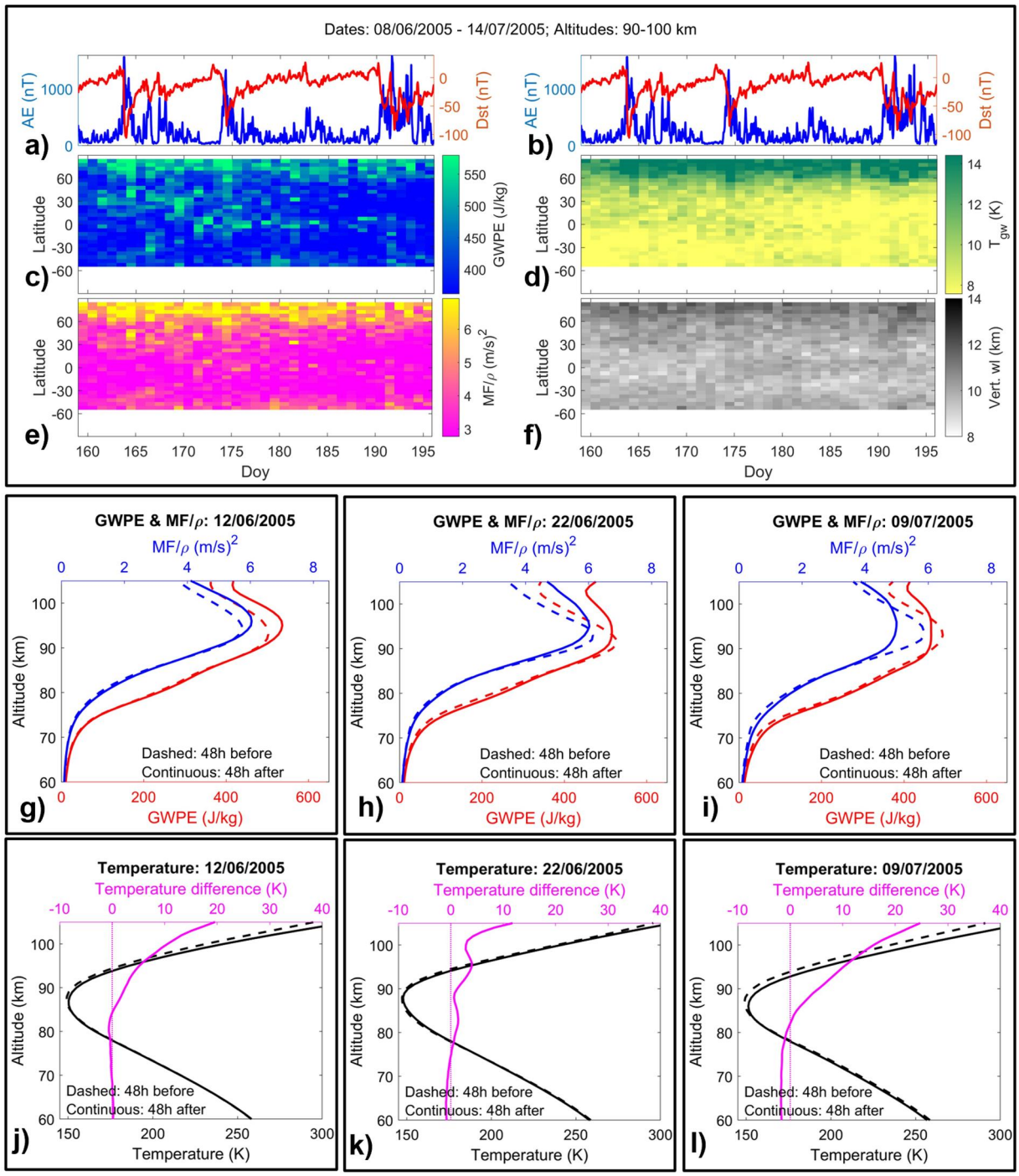

Figure 4. Events of 12 June, 22 June and 9 July 2005. (a) and (b) AE and Dst indices, (c) GWPE, (d) Temperature perturbations without subjecting to spectral analysis, (e) MF, (f) Vertical wavelengths.2. (g)-(i) Altitude profiles of zonal average GWPE and MF 48 hr before and after the geomagnetic disturbances. (j)–(l) Zonal average temperature profiles from 60 to 90° magnetic inclinations for 48 hr before and after the onset of geomagnetic event in black, and the temperature difference post and pre onset in magenta.

3.1.3. Equinoctial Observations

Figure 5 shows observations during the St. Patrick's Day storm of 17 March 2015. SABER was measuring Southern high latitudes and thus this event falls under Autumn equinox. This was the strongest geomagnetic storm of solar cycle 24. During this event, the Dst index reached −223 nT and the AE index reached 1570 nT with

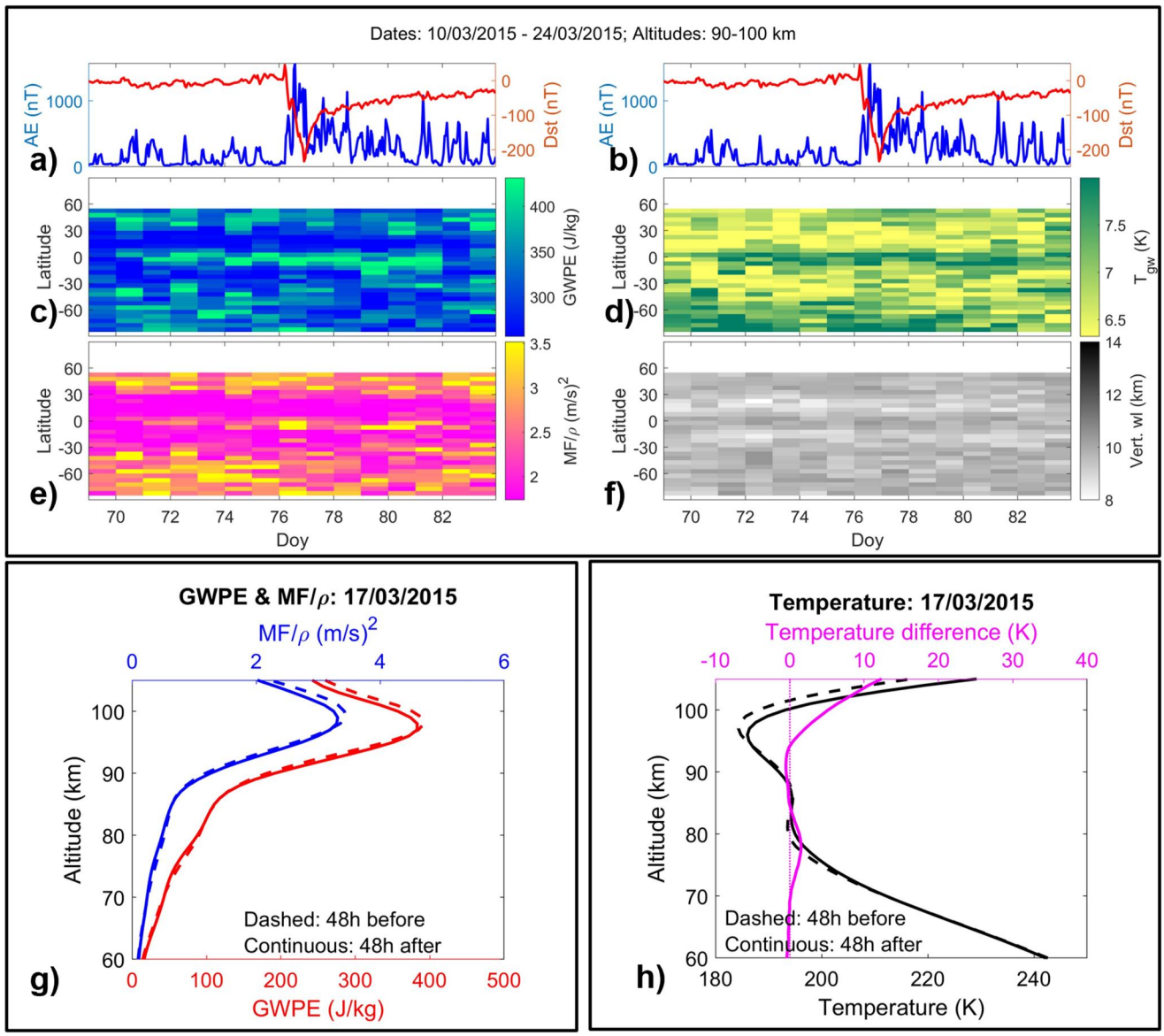

Figure 5. St. Patrick's Day storm of 17 March 2015. Figures are in the same format as that of Figure 2.

significantly high values (i.e., above 1000 nT) from 17 to 19 March 2015. However, this event did not lead to a noticeable increase in GW activity as seen from Figures 5c–5f. Figure 5g showing altitude profiles of GWPE and MF before and after the event further confirms lack of enhancement in the GW activity. This is surprising when noticing that even compound substorms have been shown to lead to enhanced GW activity (e.g., Figures 3 and 4). At the same time, Figure 5h displaying the average temperature profiles before and after the onset of the event still shows a reduction in the mesopause altitude and heating above 90 km. Nevertheless, no enhancement in GW activity is seen. It is worth noting that there was lack of response to another relatively weaker geomagnetic event on 17 March 2013, which was also observed by SABER over the southern high latitudes (not shown).

On the other hand, another autumn equinox observation during 26 September 2011 shows a noticeable enhancement in GW activity over Northern high latitudes as shown in Figure 6. This event was a compound substorm which co-occurred with a geomagnetic storm with Dst index of about −100 nT. The St. Patrick's Day storms of 2015 (Figure 5) and 2013 are more intense geomagnetic events that did not lead to an increase in GW activity. The 48 hr average temperature profile comparisons before and after the onset for the event of 26 September 2011 shown in Figure 6h indicates similar heating and a reduction in the mesopause altitude compared

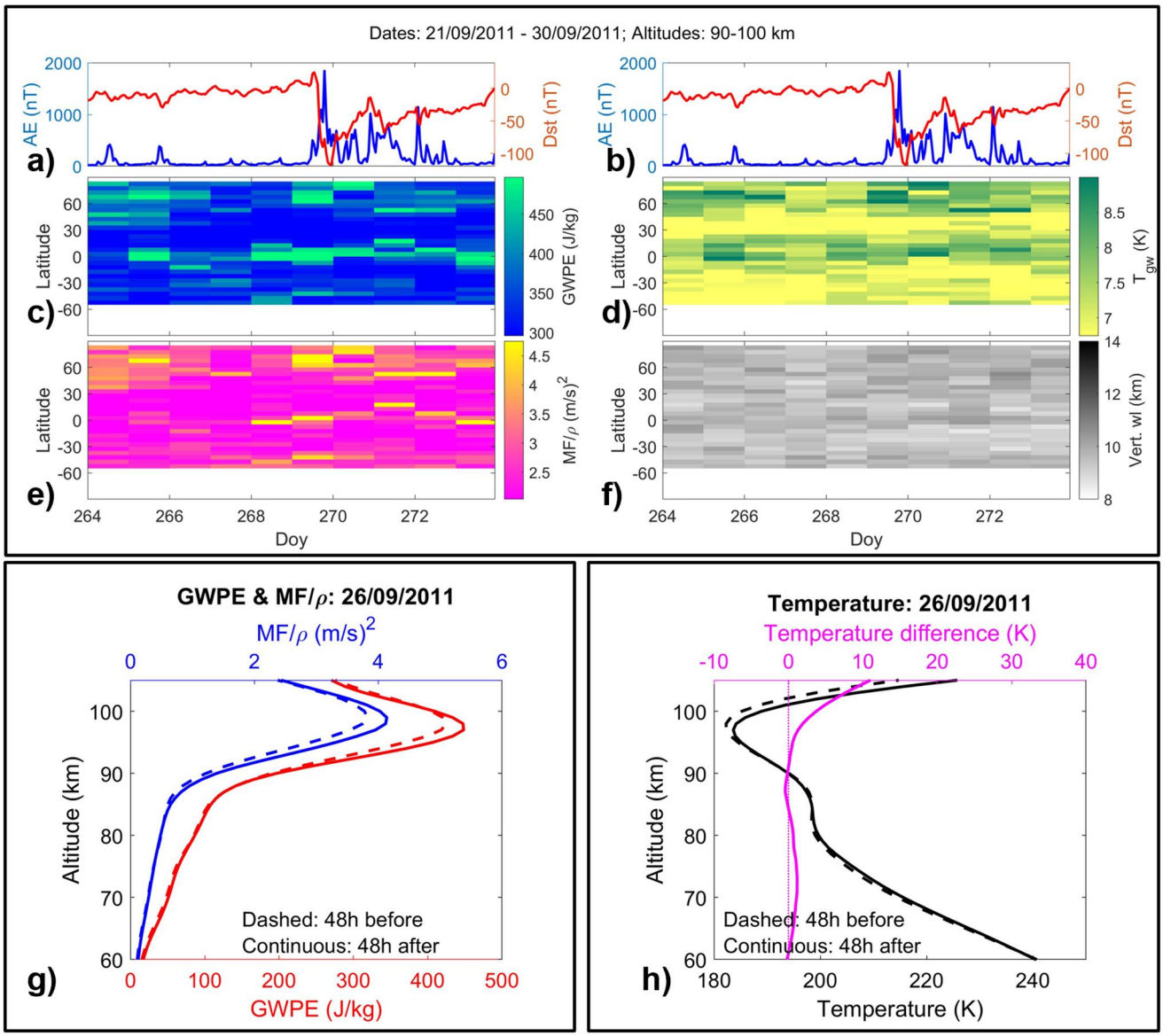

Figure 6. Autmn equinox observation showing an enhancement in GW activity. Figures are in the same format as that of Figure 2.

to 17 March 2015 event (Figure 5h). This further implies that the GW response does not merely depend on the strength of geomagnetic activity, heating associated with it or the extent of the descent of mesopause. Therefore, other factors like temperature gradient, wind variations and pre-existing wave activity play a role in the extent of enhancement in the GW activity post onset of a geomagnetic event.

Three events occurred during vernal equinox season with $AE \geq 1500$ nT, and two of them showed a clear enhancement in GW activity following the start of geomagnetic disturbance. Each hemisphere witnessed one such event (not shown).

3.2. Statistics

First, we discuss the cases where the maximum AE index is above 1500 nT or minimum Dst index below −200 nT from which the individual cases shown in the previous section are selected. Figures 7a–7c and 7d–7f shows the altitude profiles of percentage changes of GWPE and MF, respectively, for all the 24 events selected. The thin black vertical line indicates 0 and thick dashed black line corresponds to +10%, our threshold to unambiguously identify a change post onset of geomagnetic activity. The shading in the background represents values between

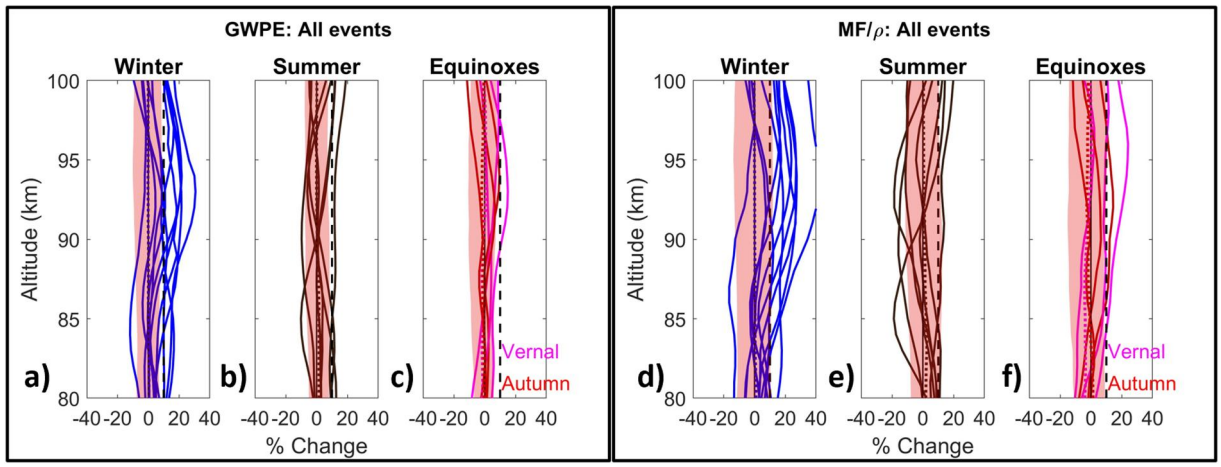

Figure 7. Percentage changes of GWPE per unit mass for (a) winter, (b) summer and (c) equinoxes, and MF per unit mass for (d) winter, (e) summer and (f) equinoxes for the events having threshold values of $AE \geq 1500$ nT or $Dst \leq -200$ nT. The region between 15th and 85th percentiles from random control calculations of 7,000 samples are shaded in the background. The dotted color line close to 0% is the median value from the control run. The thin and dashed black lines respectively show the 0 line and 10% threshold.

15th and 85th percentile from the 7,000 point random control calculations. The left edge of the patch indicates the 15th percentile while the right edge is the 85th percentile. Note that our threshold of 10% lies close to the 85th percentile. The dotted color lines for each season close to the zero line are the median values. Most of the winter cases in Figures 7a and 7d show positive excursion beyond 10% threshold in the 80–100 km altitude range, while only 1 case in summer show a such a behavior (Figures 7b and 7e). During equinoxes, 3 out of 6 events showed a positive excursion beyond 10% line for MF (Figure 7f). From Figure 7e, it appears as if there are reductions in the GW activity during summer following geomagnetic storms. However, this is not the case as will be proved with a larger data set as discussed below.

In order to increase the number of cases and ensure that the statistics discussed above hold, we proceed to analyze all events with peak AE > 1000 nT. Out of the 253 identified events, 5 occurred around the dates of SABER/TIMED yaw change and hence cannot be used, leaving 248 events for statistical analysis. For these events we calculate the percentage changes in GWPE and MF and define an average percentage change greater than 10% between 85 and 100 km altitudes as a meaningful change. The results are shown in Figure 8a for both the hemispheres and 8b and 8c respectively for the Northern and Southern hemispheres. Figure 8 shows a clear dip in summer in the response, in concurrence with our case studies (Figure 7). The responses are similar between the hemispheres. Statistically, the GW enhancements during equinoxes appear to be slightly stronger than those during the winter solstice in the Northern hemisphere than the Southern hemisphere. We also checked for significant reductions below 10% post onset of geomagnetic disturbances to see if there are significant number of cases, particularly during summer. Only about 10% of the cases showed a percentage reduction of GW activity below 10% during intense geomagnetic disturbances. They might be a reflection of the background variations of GW activity, while about 20%–60% of the cases show an enhancement in different seasons as revealed by Figure 8. Therefore, the enhancement of GW activity post onset of geomagnetic disturbances is a statistically valid result, while the reasons for why only some events show an unambiguous response needs to be investigated in the future.

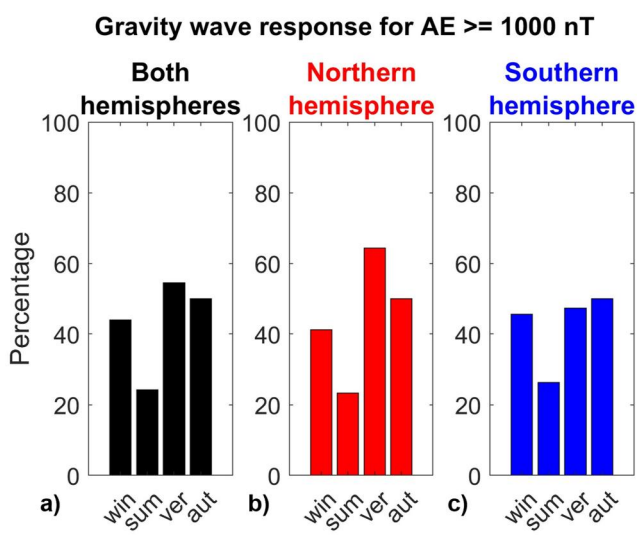

Figure 8. Seasonal and hemispherical response for geomagnetically active events having maximum $AE \geq 1000$ nT.

4. Discussion

In this section, we will consolidate the above observations and discuss the reasons for the observed seasonality in the GW response to geomagnetic activity. As seen from examples given in Figures 3, 4, and 6, we note that

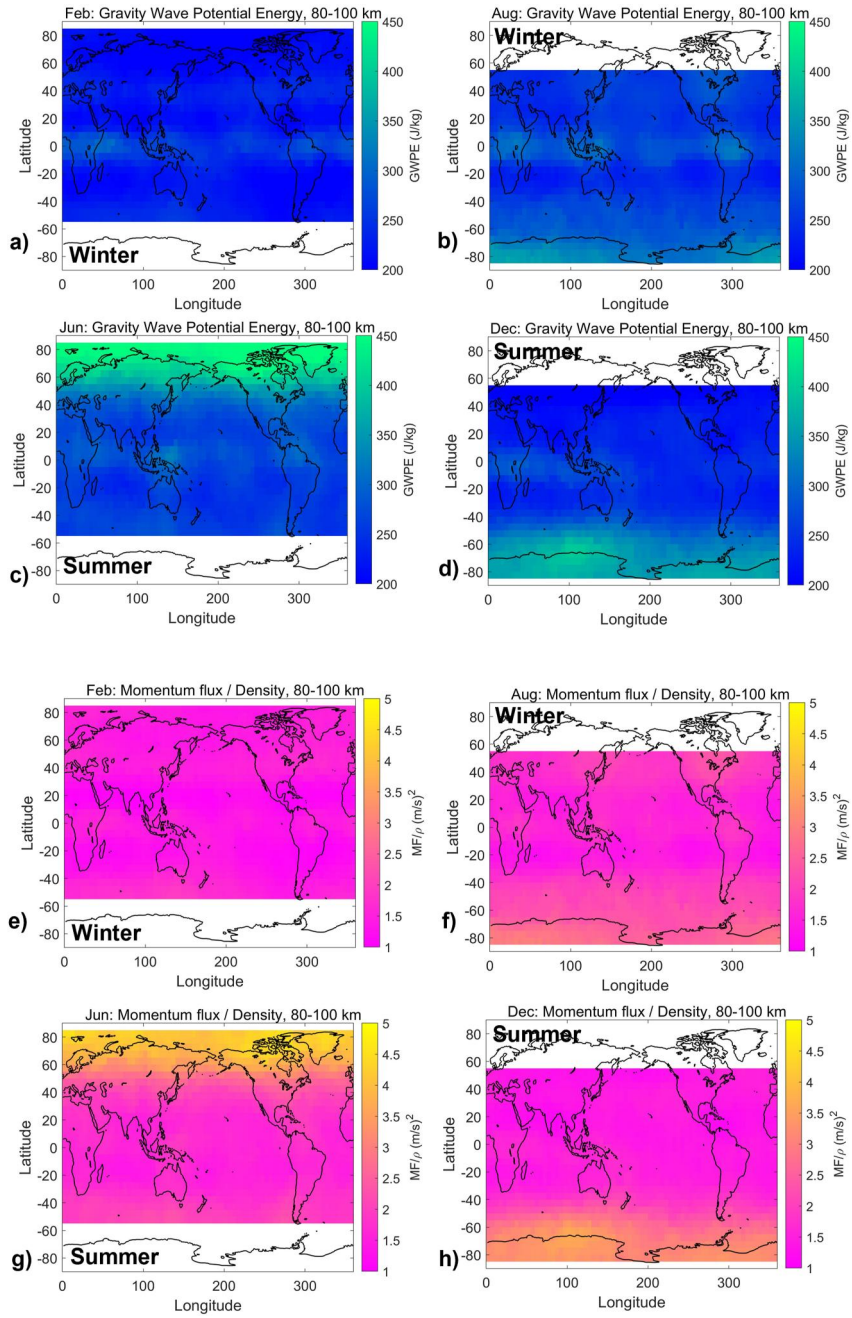

Figure 9. Climatology of GWPE (a)–(d) and MF (e)–(h). The left and right columns show Northern and Southern hemisphere climatologies, respectively. Winter season is given in (a, b, e, and f) while summer in (c, d, g, and h). Note, clear enhancements in the GW parameters in summer high latitudes and that the seasonal differences are largest in the Northern hemisphere.

intense substorm activity plays an important role in affecting the GW variability. It is known that geomagnetic disturbances may arise from different drivers such as coronal mass ejections, corotating interaction regions and high-intensity long-duration continuous AE activity (HILDCAA). We did not separate the events based on the drivers because all of them produce substorms and almost all intense geomagnetic storms co-occur with strong substorm events. The enhancement in GW activity is always observed only in the high latitude regions, and more importantly they occur in a transient manner nicely coinciding with the periods of geomagnetic disturbances as seen from AE index enhancements (Figures 2–6). This indicates that active forcing generates the GWs, that is,

they are not propagating from elsewhere. Hence substorm related heating effects appear to be the source for these GWs.

Two major GW sources in the high latitude upper atmosphere associated with geomagnetic activity are Joule and particle heating (Oyama & Watkins, 2012). Joule heating peaks in the region of 120–130 km while particle heating peaks at lower altitudes where the atmospheric density is large enough for frequent collisions. An increase in vertical wavelength coincident with the increased GW activity following geomagnetic disturbances is observed in ∼70% of the cases with peak $AE \geq 1500$ nT. This preferential formation of longer vertical wavelength GWs following geomagnetic activity might be an indication of the underlying generation mechanism. From the temperature profiles shown in Figures 2 and 4–6, it is seen that heating occurs above 90 km. This implies that particle heating is likely to be the important source responsible for the GWs observed below 100 km, because heating may occur almost in situ and immediately above the region of wave observation. Particle heating may also have a matching vertical scale length to that of observed vertical wavelengths.

The weaker summer response of GW activity to geomagnetic disturbances may be due to a combination of seasonal variations in wave forcing, temperature structure and pre-existing GW activity. If Joule heating creates a portion of the observed GWs, the extent of Joule heating will be lesser in the enhanced ionospheric conductivities of the sunlit summer high latitudes compared to other seasons. The extent of particle heating in summer below 100 km is also lesser or of comparable magnitude to the other seasons - for example, compare Figures 4j–4l with those of Figures 2h, 5h and 6h. These indicate that there is at least no excessive Joule or particle heating occurring in the summer to force significantly larger amounts of GWs than other seasons.

Note that the upper mesospheric temperature structures in the high latitudes are broadly similar during the equinoxes and winter (e.g., Figures 2h, 5, and 6). The mesopause normally occur between 95 and 100 km in non-summer high latitude region. However, during high latitude summer, it is well known that the mesopause descends to 85–90 km as seen in Figures 4j–4l. Therefore, in summer, the whole wave generation region due to the auroral heating (both Joule and particle heating) lies in a steep lower thermospheric temperature gradient that could suppress the vertical propagation of GWs. The suppression is expected due to the strong gradient in buoyancy frequency profile which inhibits propagation of the waves.

Climatologies of GWPE and MF from SABER measurements between 2002 and 2018 are shown in Figure 9. Panels (a–d) show GWPE and (e–h) show MF. The left (right) panels in the Figure show Northern (Southern) Hemispheric winter and summer seasons as alternating rows. Because of yaw changes of the TIMED satellite, coverage is poor at latitudes >55° in one of the hemispheres even in the climatological averages and hence the variations are separately shown for the Northern and Southern Hemispheres. Two aspects can be clearly seen from the Figure: (a) wave activity in summer high latitudes are significantly higher in the altitude region of 80–100 km in both the hemispheres. Already existing strong wave activity during summer may mask the contribution from geomagnetic activity compared to other seasons, resulting in a weaker summer response. (b) The extent of the difference between winter and summer is greater in the Northern Hemisphere than the Southern Hemisphere (compare Figures 9a and 9c with 9b and 9d for GWPE and Figures 9e and 9g with 9f and 9h for MF). Given that hemispheric asymmetries are an interesting contemporary research topic (Ern et al., 2022; Hong et al., 2023; Yan et al., 2021), the exact cause of such climatological differences needs further attention.

Also, the GW climatology during winter and equinoxes appears similar. We have not shown the climatologies for the equinoxes herein. Due to the yaw changes of SABER satellite, the data coverage for the climatologies for Autumn is better than those for spring. The Autumn climatologies for the month of October in the Northern hemisphere and for April in the Southern hemisphere closely resemble that of the winter climatologies in the respective hemispheres (i.e., Figures 9a and 9e are similar for climatology of October and Figures 9b and 9f for April). Therefore, the generation mechanisms, propagation conditions and pre-existing GW activity are broadly similar between the winter and equinoxes, while differing from that of summer both due to the temperature structure and due to large pre-existing GW activity.

Even during non-summer periods, the enhanced GW activity is seen only in 48% of cases. It is possible that chemical cooling effects due to nitric oxide may play a role in determining the GW response for a particular event. Improved upper-atmospheric modeling may aid understanding of the processes that lead to enhanced wave activity in some events and not in others. Moreover, a detailed study on the pattern of particle precipitations and their relationship to observed GW enhancements might provide better insights on the interplay between wave

generation and background conditions. It is recognized that each geomagnetic event is different and the effects they produce are also largely variable. With the available information on temperatures up to 110 km, we are unable to experimentally establish the underlying cause for enhanced wave forcing in some events but not on some others, irrespective of seasons.

5. Summary and Conclusion

This work shows for the first time the geographical regions and the altitudes from where the geomagnetic disturbances become an important GW source. We show that the geomagnetic activity generated GWs are dominant in the upper mesospheric region above 80 km in the high latitudes where particle precipitation along the magnetic field lines occur. The observed GW enhancements coincide with the duration of geomagnetic activity. No consistent GW enhancements are seen in the lower altitudes or latitudes below 55°. Noteworthy is the seasonality in the GW response to geomagnetic disturbances wherein the summer hemisphere showed weakest response. This appears to be due to the lower mesopause altitude in summer along with a steep temperature gradient in the 85–100 km region and larger pre-existing wave activity.

Nevertheless, the response in GW activity for geomagnetic disturbances is irregular in all the seasons in that only 42% of the cases show an unambiguous increase in the GW activity. During non-summer periods, the percentage increases slightly to 48%. Therefore, in any particular case, there is no certainty in the enhancement of GW activity. This indicates that the pre-existing GWs excited by other lower atmospheric sources and background wind and temperature conditions combine with the forcing from geomagnetic activity in determining GW variability around a particular event. Detailed case studies combining both satellite and ground based measurements will help to gain a better understanding of reason behind some events not showing significant wave enhancements despite intense geomagnetic disturbances like that of 17 March 2015 superstorm.

Data Availability Statement

The SABER/TIMED data used in this work can be obtained from https://saber.gats-inc.com/, and AE and Dst indices from https://wdc.kugi.kyoto-u.ac.jp/.

Acknowledgments
This work is supported by NERC project MesoS2D with Grants NE/V01837X/1, NE/V018426/1. CW is supported by Royal Society Fellowship URF\R\221023. NH is supported by NE/W003201/1 and NE/S00985X/1 and UKRI NERC Independent Research Fellowship NE/X017842/1. PN is supported by a NERC GW4+ Doctoral Training Partnership studentship NE/S007504/1.

References

Alexander, M. J., Gille, J., Cavanaugh, C., Coffey, M., Craig, C., Eden, T., et al. (2008). Global estimates of gravity wave momentum flux from High Resolution Dynamics Limb Sounder observations. *Journal of Geophysical Research*, *113*(D15), D15S18. https://doi.org/10.1029/2007JD008807

Alken, P., Thébault, E., Beggan, C. D., Amit, H., Aubert, J., Baerenzung, J., et al. (2021). International geomagnetic reference field: The Thirteenth generation. *Earth, Planets and Space*, *73*(1), 49. https://doi.org/10.1186/s40623-020-01288-x

Blanc, E., Ceranna, L., Hauchecorne, A., Charlton-Perez, A., Marchetti, E., Evers, L. G., et al. (2017). Toward an improved representation of middle atmospheric dynamics: Thanks to the arise project. *Surveys in Geophysics*, *39*(2), 171–225. https://doi.org/10.1007/s10712-017-9444-0

Ern, M., Preusse, P., Alexander, M. J., & Warner, C. D. (2004). Absolute values of gravity wave momentum flux derived from satellite data. *Journal of Geophysical Research*, *109*(D20), D20103. https://doi.org/10.1029/2004JD004752

Ern, M., Preusse, P., & Riese, M. (2022). Intermittency of gravity wave potential energies and absolute momentum fluxes derived from infrared limb sounding satellite observations. *Atmospheric Chemistry and Physics*, *22*(22), 15093–15133. https://doi.org/10.5194/acp-22-15093-2022

Esplin, R., Mlynczak, M. G., Russell, J., Gordley, L., & Team, T. S. (2023). Sounding of the atmosphere using broadband emission radiometry (saber): Instrument and science measurement description. *Earth and Space Science*, *10*(9), e2023EA002999. https://doi.org/10.1029/2023EA002999

Fleming, E. L., Chandra, S., Burrage, M. D., Skinner, W. R., Hays, P. B., Solheim, B. H., & Shepherd, G. G. (1996). Climatological mean wind observations from the UARS high-resolution Doppler imager and wind imaging interferometer: Comparison with current reference models. *Journal of Geophysical Research*, *101*(D6), 10455–10473. https://doi.org/10.1029/95JD01043

Fritts, D. C., & Alexander, M. J. (2003). Gravity wave dynamics and effects in the middle atmosphere. *Reviews of Geophysics*, *41*(1), 1003. https://doi.org/10.1029/2001RG000106

García-Comas, M., López-Puertas, M., Marshall, B. T., Wintersteiner, P. P., Funke, B., Bermejo-Pantaleón, D., et al. (2008). Errors in sounding of the atmosphere using broadband emission radiometry (SABER) kinetic temperature caused by non-local-thermodynamic-equilibrium model parameters. *Journal of Geophysical Research*, *113*(D24), D24106. https://doi.org/10.1029/2008JD010105

Gettelman, A., Mills, M. J., Kinnison, D. E., Garcia, R. R., Smith, A. K., Marsh, D. R., et al. (2019). The whole atmosphere community climate model version 6 (WACCM6). *Journal of Geophysical Research: Atmospheres*, *124*(23), 12380–12403. https://doi.org/10.1029/2019JD030943

Gordley, L. L., Hervig, M. E., Fish, C., Russell, J. M., Bailey, S., Cook, J., et al. (2009). The solar occultation for ice experiment. *Journal of Atmospheric and Solar-Terrestrial Physics*, *71*(3), 300–315. https://doi.org/10.1016/j.jastp.2008.07.012

Harding, B. J., Makela, J. J., Englert, C. R., Marr, K. D., Harlander, J. M., England, S. L., & Immel, T. J. (2017). The MIGHTI wind retrieval algorithm: Description and verification. *Space Science Reviews*, *212*(1–2), 585–600. https://doi.org/10.1007/s11214-017-0359-3

Harvey, V. L., Pedatella, N., Becker, E., & Randall, C. (2022). Evaluation of polar winter mesopause wind in WACCMX+DART. *Journal of Geophysical Research: Atmospheres*, *127*(15), e2022JD037063. https://doi.org/10.1029/2022JD037063

Hertzog, A., Alexander, M. J., & Plougonven, R. (2012). On the intermittency of gravity wave momentum flux in the stratosphere. *Journal of the Atmospheric Sciences*, *69*(11), 3433–3448. https://doi.org/10.1175/JAS-D-12-09.1

Hindley, N. P., Mitchell, N. J., Cobbett, N., Smith, A. K., Fritts, D. C., Janches, D., et al. (2022). Radar observations of winds, waves and tides in the mesosphere and lower thermosphere over South Georgia island (54 S, 36 W) and comparison with WACCM simulations. *Atmospheric Chemistry and Physics*, *22*(14), 9435–9459. https://doi.org/10.5194/acp-22-9435-2022

Hindley, N. P., Wright, C. J., Smith, N. D., Hoffmann, L., Holt, L. A., Alexander, M. J., et al. (2019). Gravity waves in the winter stratosphere over the southern ocean: High-resolution satellite observations and 3-d spectral analysis. *Atmospheric Chemistry and Physics*, *19*(24), 15377–15414. https://doi.org/10.5194/acp-19-15377-2019

Hong, Y., Deng, Y., Zhu, Q., Maute, A., Hairston, M. R., Waters, C., et al. (2023). Inter-hemispheric asymmetries in high-latitude electrodynamic forcing and the thermosphere during the October 8-9, 2012, geomagnetic storm: An integrated data -model investigation. *Frontiers in Astronomy and Space Sciences*, *10*. https://doi.org/10.3389/fspas.2023.1062265

Hunsucker, R. D. (1982). Atmospheric gravity waves generated in the high-latitude ionosphere: A review. *Reviews of Geophysics*, *20*(2), 293–315. https://doi.org/10.1029/RG020i002p00293

Jin, H., Miyoshi, Y., Fujiwara, H., Shinagawa, H., Terada, K., Terada, N., et al. (2011). Vertical connection from the tropospheric activities to the ionospheric longitudinal structure simulated by a new Earth's whole atmosphere-ionosphere coupled model. *Journal of Geophysical Research*, *116*(A1), A01316. https://doi.org/10.1029/2010JA015925

John, S. R., & Kumar, K. K. (2012). TIMED/SABER observations of global gravity wave climatology and their interannual variability from stratosphere to mesosphere lower thermosphere. *Climate Dynamics*, *39*(6), 1489–1505. https://doi.org/10.1007/s00382-012-1329-9

McDonald, A. J. (2012). Gravity wave occurrence statistics derived from paired COSMIC/FORMOSAT3 observations. *Journal of Geophysical Research*, *117*(D15), D15106. https://doi.org/10.1029/2011JD016715

McLandress, C., Shepherd, G. G., Solheim, B. H., Burrage, M. D., Hays, P. B., & Skinner, W. R. (1996). Combined mesosphere/thermosphere winds using WINDII and HRDI data from the Upper Atmosphere Research Satellite. *Journal of Geophysical Research*, *101*(D6), 10441–-10453. https://doi.org/10.1029/95JD01706

Mertens, C. J., Russell III, J. M., Mlynczak, M. G., She, C.-Y., Schmidlin, F. J., Goldberg, R. A., et al. (2009). Kinetic temperature and carbon dioxide from broadband infrared limb emission measurements taken from the TIMED/SABER instrument. *Advances in Space Research*, *43*(1), 15–27. https://doi.org/10.1016/j.asr.2008.04.017

Narayanan, V. L., Gurubaran, S., & Emperumal, K. (2012). Nightglow imaging of different types of events, including a mesospheric bore observed on the night of February 15, 2007 from Tirunelveli (8.7 N). *Journal of Atmospheric and Solar-Terrestrial Physics*, *78–79*, 70–83. https://doi.org/10.1016/j.jastp.2011.07.006

Noble, P., Hindley, N., Wright, C., Cullens, C., England, S., Pedatella, N., et al. (2022). Interannual variability of winds in the Antarctic mesosphere and lower thermosphere over rothera (67Â°S, 68Â°W) in radar observations and WACCM-X. *Atmospheric Chemistry and Physics Discussions*, *2022*, 1–29. https://doi.org/10.5194/acp-2022-150

Oyama, S., & Watkins, B. J. (2012). Generation of atmospheric gravity waves in the polar thermosphere in response to auroral activity. *Space Science Reviews*, *168*(1–4), 463–473. https://doi.org/10.1007/s11214-011-9847-z

Ramkumar, T., Gurubaran, S., & Rajaram, R. (2002). Lower E-region MF radar spaced antenna measurements over magnetic equator. *Journal of Atmospheric and Solar-Terrestrial Physics*, *64*(12), 1445–1453. https://doi.org/10.1016/S1364-6826(02)00108-6

Reid, I. M. (2015). MF and HF radar techniques for investigating the dynamics and structure of the 50 to 110 km height region: A review. *Progress in Earth and Planetary Science*, *2*(1), 33. https://doi.org/10.1186/s40645-015-0060-7

Remsberg, E. E., Marshall, B. T., Garcia-Comas, M., Krueger, D., Lingenfelser, G. S., Martin-Torres, J., et al. (2008). Assessment of the quality of the Version 1.07 temperature-versus-pressure profiles of the middle atmosphere from TIMED/SABER. *Journal of Geophysical Research*, *113*(D17), D17101. https://doi.org/10.1029/2008JD010013

Roble, R. G., & Ridley, E. C. (1994). A thermosphere-ionosphere-mesosphere-electrodynamics general circulation model (Time-GCM): Equinox solar cycle minimum simulations (30–500 km). *Geophysical Research Letters*, *21*(6), 417–420. https://doi.org/10.1029/93GL03391

Shepherd, G. G., Thuillier, G., Cho, Y.-M., Duboin, M.-L., Evans, W. F. J., Gault, W. A., et al. (2012). The wind imaging interferometer (WINDII) on the upper atmosphere research satellite: A 20 year perspective. *Reviews of Geophysics*, *50*(2), RG2007. https://doi.org/10.1029/2012RG000390

Siskind, D. E., Jones, J. M., Drob, D. P., McCormack, J. P., Hervig, M. E., Marsh, D. R., et al. (2019). On the relative roles of dynamics and chemistry governing the abundance and diurnal variation of low-latitude thermospheric nitric oxide. *Annales Geophysicae*, *37*(1), 37–48. https://doi.org/10.5194/angeo-37-37-2019

Smith, A. K. (2012). Global dynamics of the MLT. *Surveys in Geophysics*, *33*(6), 1177–1230. https://doi.org/10.1007/s10712-012-9196-9

Smith, A. K., Pedatella, N. M., Marsh, D. R., & Matsuo, T. (2017). On the dynamical control of the mesosphere - Lower thermosphere by the lower and middle atmosphere. *Journal of the Atmospheric Sciences*, *74*(3), 933–947. https://doi.org/10.1175/JAS-D-16-0226.1

Stober, G., Kuchar, A., Pokhotelov, D., Liu, H., Liu, H.-L., Schmidt, H., et al. (2021). Interhemispheric differences of mesosphere-lower thermosphere winds and tides investigated from three whole-atmosphere models and meteor radar observations. *Atmospheric Chemistry and Physics*, *21*(18), 13855–13902. https://doi.org/10.5194/acp-21-13855-2021

Stockwell, R., Mansinha, L., & Lowe, R. (1996). Localization of the complex spectrum: The S transform. *IEEE Transactions on Signal Processing*, *44*(4), 998–1001. https://doi.org/10.1109/78.492555

Wright, C. J., & Gille, J. C. (2013). Detecting overlapping gravity waves using the S-Transform. *Geophysical Research Letters*, *40*(9), 1850–1855. https://doi.org/10.1002/grl.50378

Wright, C. J., Hindley, N. P., Moss, A. C., & Mitchell, N. J. (2016). Multi-instrument gravity-wave measurements over Tierra del Fuego and the Drake Passage - Part 1: Potential energies and vertical wavelengths from AIRS, COSMIC, HIRDLS, MLS-Aura, SAAMER, SABER and radiosondes. *Atmospheric Measurement Techniques*, *9*(3), 877–908. https://doi.org/10.5194/amt-9-877-2016

Wright, C. J., Rivas, M. B., & Gille, J. C. (2011). Intercomparisons of HIRDLS, COSMIC and SABER for the detection of stratospheric gravity waves. *Atmospheric Measurement Techniques*, *4*(8), 1581–1591. https://doi.org/10.5194/amt-4-1581-2011

Wu, C., & Ridley, A. J. (2023). Comparison of TIDI line of sight winds with ICON-MIGHTI measurements. *Journal of Geophysical Research: Space Physics*, *128*(2), e2022JA030910. https://doi.org/10.1029/2022JA030910

Yan, X., Konopka, P., Hauck, M., Podglajen, A., & Ploeger, F. (2021). Asymmetry and pathways of inter-hemispheric transport in the upper troposphere and lower stratosphere. *Atmospheric Chemistry and Physics*, *21*(9), 6627–6645. https://doi.org/10.5194/acp-21-6627-2021

Zawdie, K., Belehaki, A., Burleigh, M., Chou, M.-Y., Dhadly, M. S., Greer, K., et al. (2022). Impacts of acoustic and gravity waves on the ionosphere. *Frontiers in Astronomy and Space Sciences*, *9*. https://doi.org/10.3389/fspas.2022.1064152